Shape Estimation of Concentric Tube Robots Using Single Point Position Measurement

Shape Estimation of Concentric Tube Robots Using Single Point Position Measurement

Emile Mackute[1,2], Balint Thamo[1,2], Kevin Dhaliwal[2], Mohsen Khadem[1,2]

***Abstract*— Accurate shape estimation of concentric tube robots (CTRs) using mathematical models remains a challenge, reinforcing the need to develop techniques for accurate and real-time shape sensing of CTRs. In this paper, we develop a fusion algorithm that predicts the robot's shape by combining a mathematical model of the CTR with a measurement of the Cartesian coordinates of the robot's tip using an electromagnetic sensor. We experimentally validated our method in static and dynamic scenarios with and without external loading. Results demonstrated that the fusion algorithm improves the error of model-based shape prediction by an average of 44.3%, corresponding to 2.43% of the robot's arc length. Furthermore, we demonstrate that our method can be used in real-time to simultaneously track the robot's tip position and predict its shape.**

I. INTRODUCTION

Concentric tube robot (CTR) is a type of continuum robot comprised of several concentrically nested pre-curved Nitinol tubes. Tubes can make translational and rotational movements that change the robot's shape and tip pose [1]. As opposed to discrete joint robots, CTRs have continuously bending curvature that allows them to generate smooth curvilinear motions and follow tightly curved trajectories in small confined spaces. Accurate manipulation and control of CTRs require the knowledge of their tip position and shape, specifically when the robot operates near susceptible tissues and organs or when the desired target is obscured by anatomical obstacles [2]. Here, we propose an accurate and robust sensing algorithm which can estimate CTRs' shape on the fly, under large deflections, and in the presence of unknown external forces using only the measurement of the Cartesian coordinates of the robot's endpoint.

A. Related Work

The shape of CTRs can be described by kinematic/dynamic models relating the shape of the robot's backbone to the robot's joint inputs. The most common approach for modeling CTRs is using the Cosserat rod theory [3], [4]. However, model-based shape sensing often has large errors. It requires accurate knowledge of external forces, which is not always available. Moreover, highly non-linear kinematics, torsion, and friction limit the models' accuracy.

Electromagnetic (EM) trackers are commonly used to measure the position of continuum robots [2]. EM tracking uses mutual induction between a magnetic field generator and a magnetic field tracker placed on the robot to measure the tracker's position and orientation. However, estimating the overall shape of the robot requires numerous trackers, which limits EM tracking application in shape sensing.

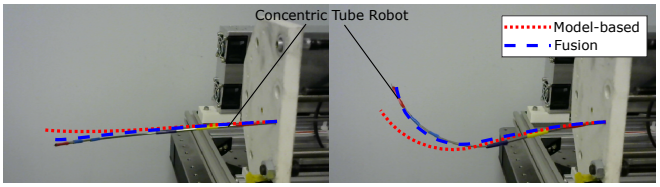

Fig. 1. A comparison of the proposed shape estimation algorithm with the shape of the robot estimated using the kinematic model of CTR [4].

Some researchers have investigated intraoperative imaging modalities such as fluoroscopy to track the shape of continuum robots. In [5], a monoplane C-arm was used to obtain a set of images which were combined with a kinematic model to improve the shape estimate of a continuum robot. In [6], monoplane X-ray fluoroscopy images were fused with model-based shape estimations. The method was later improved by employing Markov Random Fields to unify shape estimation and tracking tasks [7]. The downside of using imaging to estimate the robot's shape is the exposure of patients to a large amount of radiation. Additionally, image-based methods suffer from line of sight occlusions.

Fibre-Bragg gratings (FBGs) sensors are another popular shape sensing modality. FBG fibres allow shape estimation by measuring strain on various points along the robot's backbone. Some authors have been able to determine the shape of flexible needles and continuum robots by combining 3 FBG fibres into a curvature sensor [8]–[12]. Multi-core fibres have produced even greater accuracy by removing the need to manually position the fibres [13].

Several researchers have fused the previous methods to provide more accurate and reliable shape sensing. In [14], an extended Kalman filter is proposed to fully track the shape of a highly articulated snake robot. The filter combined the kinematic model of the snake to predict the position and orientation of each link, and an EM sensor at the tip of the snake to update the estimation. While EM can only track the position of a single point, it was sufficient to fully observe the snake's state due to its follow-the-leader steering mechanism. Similarly, [15] used a Kalman filter to combine the needle deflection model with an EM sensor to improve the needle's tip position measurement.

In another work [16], two algorithms, namely, Luenberger observer and Kalman filter, are used to track the tip of a magnetically actuated catheter. Both estimators combine FBG shape sensing and ultrasound tracking. The shape from FBG

This work was supported by the Medical Research Council [MR/T023252/1].

[1]School of Informatics, University of Edinburgh, UK.

[2]The Translational Healthcare Technologies Group in Centre for Inflammation Research, The Queen's Medical Research Institute, University of Edinburgh, UK

sensors was used to recover the tip position of the catheter, while it was also tracked in the ultrasound image using either template-matching or convolutional neural network-based tracking. A similar approach was implemented in [17] to track the tip of a continuum manipulator in a 2D plane with a Kalman filter, combining FBG sensors and simulated low radiation fluoroscopy imaging.

B. Motivation and Contributions

Safe deployment and control of CTRs for surgical interventions require accurate measurement of robots' shape. Model-based shape sensing has relatively large errors. FBG-based shape sensing still faces challenges that hinder its mainstream use. FBGs have been tested on needles [8]–[12] or robots with a small arc length [17], [18] as they offer low accuracy in high deflection structures [2]. Moreover, the relatively high cost of fibre assembly and data acquisition systems limit their widespread application.

In this paper, we present a fusion algorithm that employs a kinematic model of the CTR and an EM-based position measurement of the robot's tip to provide an accurate and reliable estimation of a concentric tube robot's shape (Fig. 1). The proposed method only relies on the position measurement of a single point on the robot's tip using a commercially available EM tracker and does not suffer from the aforementioned drawbacks of model-based and FBG-based shape estimation approaches. Experiments are performed to validate the proposed approach in both static and dynamic settings. The results demonstrate that the proposed algorithm is capable of predicting the robot's shape with a mean error corresponding to 2.38% of the robot's arc length when the robot is in free space and a mean error of 2.45% when the robot is under external forces. Our algorithm is available online [1].

II. Methodology

We present a fusion algorithm for the shape estimation of CTRs. The algorithm employs a nonlinear observer that combines the information from the kinematic model of the robot and the EM-based position measurement. The kinematic model is based on the Cosserat rod theory and was developed in [3], [4].

Fig. 2(a) shows a schematic of a CTR. Shape of the robot can be described by a continuous curve parameterized by its arc length s. Additionally, a sliding Bishop frame is assigned continuously at each point on the curve, with its d_3 axis always tangent to the curve. The configuration of the rod at a time t can be defined using a unique set of 3D centroids, $r(s,t) : [0,\ell] \times [0,\infty] \to \mathbb{R}^3 \times [0,\infty]$, and a family of orthogonal transformations, $R(s,t) : [0,\ell] \times [0,\infty] \to SO(3) \times [0,\infty]$. Finally, $u(s,t) : [0,l] \times [0,\infty] \to \mathbb{R}^3 \times [0,\infty]$ defines the curvature of the rod.

As mentioned before, due to the modeling inaccuracies such as unknown external forces, friction, or nonlinear phenomena such as twist in the body of the rod, the model-based shape prediction is inaccurate. We hypothesize that by

[1] https://github.com/SIRGLab/CTR-Shape-Estimation

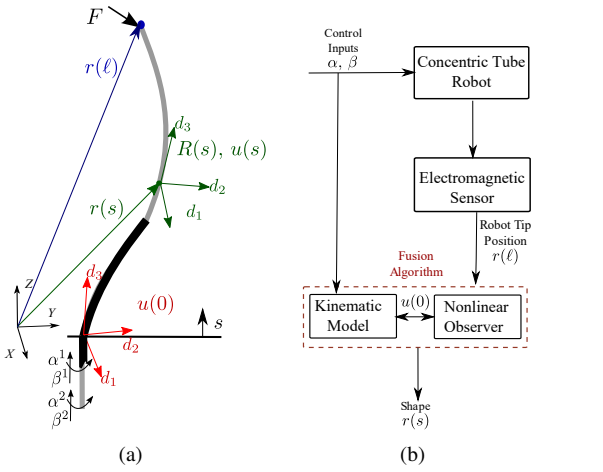

Fig. 2. (a) A schematic of a CTR with two tubes under external force, F. CTR is modelled as a deformable curve with a frame attached to every point along its arc length s, with the d_3 axis of the frame remaining tangent to the curve. $r(s)$, $R(s)$, and $u(s)$ denote the position, rotation, and the instantaneous curvature of the rod at arc length s, respectively. The actuation variables α and β denote the rotation, and translation of the tube's base, respectively. (b) Block diagram of the fusion algorithm.

accurately measuring the correct initial curvature of the rod at its base $u(0,t)$, we can estimate the effects of the modelling inaccuracies on the deflection of the robot. Following this hypothesis, we design a nonlinear state observer that accepts the robot tip position $r(\ell,t)$ as an input and predicts the correct initial curvature of the rod $u(0,t)$ as an output. This estimation is passed on to the kinematic model to predict the shape of the rod $r(s,t)$ while compensating for modelling inaccuracies. The block diagram of the proposed algorithm is shown in Fig. 2(b). In the remainder of this section, we present a description of the CTR model and detail the design of the fusion algorithm composed of a nonlinear observer and the kinematic model of CTR. In the equations we use prime and dot symbols to denote a first order derivative with respect to space variable s and time variable t, respectively.

A. CTR Model Overview

Following the terminology shown in Fig. 2(a), each concentric tube is described by $r^i(s,t)$, $R^i(s,t)$, and $u^i(s,t)$, where $i = 1, \cdots, N$ corresponds to the number of the tube, starting from the innermost tube. Furthermore, with tube 1 being the longest, we consider $r^1(s,t)$ to be equal to the curve of the robot. Its kinematic model is given by (1):

$$r^{1\prime}(s,t) = R^1(s,t)e_3, \tag{1a}$$

$$R^{1\prime}(s,t) = R^1(s,t)[u^1(s,t)]_\times, \tag{1b}$$

$$\begin{aligned} u_n^{1\prime}(s,t) = -\Bigg(\sum_{i=1}^{N} K^i\Bigg)^{-1} \sum_{i=1}^{N} R_{\theta^i} \Bigg[& \\ K^i\big(\theta^{i\prime}\frac{dR_{\theta^i}{}^T(s,t)}{d\theta^i}u^1(s,t) - U^{i\prime}\big) & \\ + [u^{i\prime}(s,t)]_\times K^i\big(u^i(s,t) - U^i\big)\Bigg] & \\ - \Bigg(\sum_{i=1}^{N} K^i\Bigg)^{-1} \Big[[e_3]_\times R^{1T}(s,t)F(t)\Big]\Big|_{n=1,2}, & \end{aligned} \tag{1c}$$

$$u_3^{i\,\prime}(s,t) = \frac{E^i I^i}{G^i J^i}\big(u_1^i(s,t)U_2^i - u_2^i(s,t)U_1^i\big), \tag{1d}$$

$$u_n^{i\,\prime}(s,t) = {R_{\theta^i}}^T(s,t)u^1(s,t) + \theta^{i\prime}(s,t)e_3\Big|_{n=1,2}, \tag{1e}$$

$$\theta^{i\prime}(s,t) = u_3^i(s,t) - u_3^1(s,t), \tag{1f}$$

where $e_3 = [0\ 0\ 1]^T$ is a unit vector and the $[.]_\times$ operator is the isomorphism between a vector in $\mathbb{R}^3$ and its skew-symmetric cross product matrix. $K^i = diag(E^iI^i, E^iI^i, G^iJ^i)$ is the stiffness matrix of the i^{th} tube where E^i corresponds to the tube's Young's modulus, I^i is its second moment of inertia, G^i is its shear modulus, and J^i is the tube's polar moment of inertia. U^i is the known pre-curvature of i^{th} tube and $F(t)$ is the external force vector. Finally, θ^i is the twist angle of the i^{th} tube about the z-axis with respect to the global frame.

The ODE system in (1) has the following boundary conditions:

$$r^1(0,t) = [0\ 0\ 0]^T, \tag{2a}$$

$$R^1(0,t) = R_z(\theta^1(t)) = \begin{bmatrix}\cos(\theta^1(t)) & -\sin(\theta^1(t)) & 0\\ \sin(\theta^1(t)) & \cos(\theta^1(t)) & 0\\ 0 & 0 & 1\end{bmatrix}, \tag{2b}$$

$$\theta^i(0,t) = \alpha^i(t) - \beta^i(t)u_3^i(0,t), \tag{2c}$$

$$u^i(\ell^i + \beta^i(t), t) = U^i. \tag{2d}$$

Here, $\alpha(t)$ and $\beta(t)$ are the actuation values at a time step t, rotation and translation respectively. ℓ^i is the length of tube i.

The model given in (1) is quasi-static. It is assumed that at a given time, time-dependent variables are constant and the equations are solved with respect to s. To solve the boundary value problem, shooting methods can be used. A shooting method consists of using a nonlinear root-finding algorithm to iteratively converge on values for $u(0,t)$, in order to satisfy (2). Next, the time-dependent variables are updated (*i.e.* $\alpha^i(t)$, $\beta^i(t)$), and the equations are solved again in the spatial domain.

B. Curvature Observer

Here, we design a nonlinear observer to estimate the robot shape, assuming that the robot tip position is known. The mathematical model of the robot given in Sec. II-A is inaccurate due to the existence of disturbances such as friction and unknown loads. Our main hypothesis is that the disturbances cause the robot shape and initial curvature to deviate from model prediction. Thus, we can estimate the effects of the modelling inaccuracies on the deflection of the robot by updating the initial curvature of the robot at its base $u(0,t)$ via sensor measurements. To this end, we propose a nonlinear observer that accepts the robot's tip position $r(\ell)$ at the time t as an input and predicts the curvature of the robot at its base $u(0,t)$. The observer aims to estimate $u(0,t)$ over time while minimizing the error between the robot's tip position and an EM-based measurement defined as

$$\epsilon(t) = r^1(\ell,t) - r^s, \tag{3}$$

where r^s denotes sensor's measurements.

To design the observer, let us first define an auxiliary variable C:

$$C := \frac{\partial r^1(s,t)}{\partial u(0,t)}, \tag{4}$$

where $u(0,t)$ is a $N+2$ dimensional vector consisting the first tube's initial curvature and the initial twist curvatures of all other tubes:

$$u(0,t) = [u_1^1(0,t),\ u_2^1(0,t),\ u_3^1(0,t),\ u_3^2(0,t),\ ...\ u_3^N(0,t)]^T \tag{5}$$

and N is the total number of tubes.

Now, we can take the time derivative of the observer prediction error given in (3) and obtain:

$$\dot\epsilon(t) = C(\ell + \beta(t), t)\dot u(0,t) - \dot r^s(t). \tag{6}$$

Equation (6) is a first-order linear system of equations and can be optimised using the Riccati equations [19] to estimate the initial curvature $u(0,t)$ that minimises the prediction error of the observer $\epsilon(t)$ over time. The optimal solution is given as

$$u(0,t) = -\int_0^t PC^T(\ell + \beta(t), t)V\epsilon(t)\mathrm{d}t, \tag{7}$$

where $P(t)$ is the solution of the differential Riccati equation

$$\begin{aligned} -\dot P(t) &= -P(t)C^T(\ell + \beta(t), t)VC(\ell + \beta(t), t)P(t) + Q,\\ P(t_f) &= P_0, \end{aligned} \tag{8}$$

Q, V, and P_0 are all symmetric positive definite matrices. At each time step, $\epsilon(t)$ and $C(\ell + \beta(t), t)$ are updated, then $u(0,t)$ is determined by solving (7) and (8).

So far, we have shown that given the value of C, one can design an observer to estimate initial curvature of the robot and update the robot shape accordingly. To find C, we transform the kinematics model given in (1) into an observable form. We define some additional partial derivatives, namely, D, Γ, and Z:

$$D := \frac{\partial R^1(s,t)}{\partial u(0,t)}, \quad \Gamma^i := \frac{\partial u^i(s,t)}{\partial u(0,t)}, \quad Z^i := \frac{\partial \theta^i(s,t)}{\partial u(0,t)}. \tag{9}$$

We then take a partial derivative of the robot's model in (1a) with respect to $u(0,t)$:

$$\frac{\partial r^{1\prime}(s,t)}{\partial u(0,t)} = \frac{\partial R^1(s,t)e_3}{\partial u(0,t)} = {e_3}^T\frac{\partial R^1(s,t)}{\partial u(0,t)} = {e_3}^T D(s,t) \tag{10}$$

Given that s and $u(0,t)$ are mutually independent, we can switch the order or differentiation and show that (10) is equal to $C'(s,t)$:

$$C'(s,t) = \left(\frac{\partial r^1(s,t)}{\partial u(0,t)}\right)' = \frac{\partial r^{1\prime}(s,t)}{\partial u(0,t)} = {e_3}^T D(s,t) \tag{11}$$

Continuing the same pattern for D, Γ, and Z, and taking partial derivative of (1), we obtain a new system of ODEs:

$$C' = {e_3}^T D, \tag{12a}$$

$$D' = [u^1]_\times^T D + \left(R^1 (T_3^1)^T\right)^T, \tag{12b}$$

$$\begin{aligned}{\Gamma_n^1}' = &-\left(\sum_{i=1}^{N} K^i\right)^{-1}\Bigg[\sum_{i=1}^{N}\Bigg[\Bigg(K^i\big({\theta^i}'\frac{d{R_{\theta^i}}^T}{d\theta^i}u^1 - {U^i}'\big) \\ &+ [u^i]_\times K^i\big(u^i - U^i\big)\Bigg)^T T_1^i\Bigg] \\ &+ \sum_{i=1}^{N} R_{\theta_i}\Big[K^i T_2^i + \big(K^i(u^i - U^i)\big)^T T_3^i + [u^i]_\times K^i \Gamma^i\Big]\Bigg], \\ &- \left(\sum_{i=1}^{N} K^i\right)^{-1}\Big[[e_3]_\times F(t) D^T\Big]\Bigg|_{n=1,2}\end{aligned} \tag{12c}$$

$${\Gamma_3^i}' = \frac{E^i I^i}{G^i J^i}\big(\Gamma_1^i U_2^i - \Gamma_2^i U_1^i\big), \tag{12d}$$

$${\Gamma_n^i}' = {u_1}^T {T_1}^T + {R_{\theta^i}}^T \Gamma^1\Big|_{n=1,2}, \tag{12e}$$

$${Z^i}' = \Gamma_3^i - \Gamma_3^1. \tag{12f}$$

In (12), we removed the (s,t) notation for simplicity. Furthermore, the terms T_1, T_2, T_3, and T_4 are partial derivatives of the terms in (1c), defined as

$$\begin{aligned} T_1^i &:= \frac{\partial R_{\theta_i}(s,t)}{\partial u(0,t)}, \quad T_2^i := \frac{\partial\big({\theta^i}'\frac{\partial {R_{\theta^i}}^T(s,t)}{\partial \theta^i}u^1(s,t)\big)}{\partial u(0,t)}, \\ T_3^i &:= \frac{\partial [u^i(s,t)]_\times}{\partial u(0,t)}, \quad T_4^i := \frac{\partial \frac{d{R_{\theta^i}}^T}{d\theta^i}}{\partial u(0,t)}. \end{aligned} \tag{13}$$

These variables can be expressed in terms of Γ and Z:

$$T_1^i = \frac{dR_{\theta^i}}{d\theta^i} Z^i, \tag{14a}$$

$$T_2^i = \frac{d{R_{\theta^i}}^T}{d\theta^i} u^1 {Z^i}' + {\theta^i}' {u^1}^T T_4^i + {\theta^i}' \frac{d{R_{\theta^i}}^T}{d\theta^i}\Gamma^i, \tag{14b}$$

$$T_3^i = \frac{\partial [u^i(s,t)]_\times}{\partial u^i(s,t)}\Gamma^i, \tag{14c}$$

$$T_4^i = \frac{d^2 {R_{\theta^i}}^T}{d{\theta^i}^2} Z^i. \tag{14d}$$

In the process of deriving (12) and (14), we used the model given in (1), chain rule, and the following definitions.

Definition 1. *Given a vector $x : \mathbb{R}^l$ and a differentiable matrix $M(x) : \mathbb{R}^l \to \mathbb{R}^{m\times n}$, let $J(x) \in \mathbb{R}^{m\times n\times l}$ be a partial derivative of $M(x)$ w.r.t x. Then*

$$J_{ijk}(x) = \frac{\partial M_{ij}(x)}{\partial x_k}. \tag{15}$$

Definition 2. *Let $F(x) : \mathbb{R}^l \to \mathbb{R}^{m\times n}$ and $G(x) : \mathbb{R}^l \to \mathbb{R}^{n\times o}$ be differentiable matrices. Then*

$$\frac{\partial (F(x)G(x))}{\partial x} = G^T(x) @ \frac{\partial F(x)}{\partial x} + \left(F(x) @ \left(\frac{\partial G(x)}{\partial x}\right)^T\right)^T, \tag{16}$$

where the transpose operation ^{T} in 3-D case is defined by $F_{ijk}^T = F_{jik}$. Operator @ indicates a product of two arrays such that if F, G and H are all 3-D matrices, then $H = F@G$ is defined as

$$H_{ijl} = \sum_{k=1}^{n} F_{ijk} \cdot G_{ikl}, \tag{17}$$

If any of the two arguments is a 2-D matrix, the first index is broadcast:

$$H_{ijl} = \sum_{k=1}^{n} F_{jk} \cdot G_{ikl}. \tag{18}$$

The initial conditions for the system in (12) are:

$$C(0,t) = \mathbb{0}_{3\times(N+2)}, \tag{19a}$$

$$D(0,t) = \mathbb{0}_{3\times 3\times(N+2)}, \tag{19b}$$

$$\Gamma^1(0,t)_{mn} = \delta_{mn}, \tag{19c}$$

$$\Gamma^i(0,t)_{mn} = \begin{cases} 1, & \text{if } m = 3 \text{ and } n = i+2, \\ 0, & \text{otherwise.} \end{cases}\Bigg|_{i=2,3,\ldots,N}, \tag{19d}$$

$$Z^i(0,t) = \mathbb{0}_{1\times(N+2)}. \tag{19e}$$

The observable CTR model now consists of the differential equations in (1) and (12) which can be solved simultaneously using initial values (2) and (19). The model can be summarised as:

$${r^1}'(s,t) = f(R,u), \tag{20a}$$

$$C'(s,t) = h(D, \Gamma^i, Z^i, T^i, R, u). \tag{20b}$$

By solving (20), we can estimate $r(\ell+\beta(t),t)$ and $C(\ell+\beta(t),t)$.

To find the shape of the CTR, first the equations in (1) and (12) are solved with respect to s given the initial values in (2a-2c) and (19). Then, $u(0,t)$ is updated through (7) and (8). The process is iterated over time until the error $\epsilon(t)$ converges. At the first time step, the initial curvature $u(0,t)$ of the robot is assumed to be zero.

III. EXPERIMENTS

Here, several experiments are performed to evaluate the accuracy of the shape estimation strategy. The observer was tested on a Dell Latitude 5580 laptop with Intel(R) Core(TM) i7-7600U CPU processor and 16.0 GB RAM. The experimental setup consists of a concentric tube robot with two tubes and a 5-DOF EM sensor (Aurora, NDI) attached to its tip (Fig. 3). Independent shape measurements are acquired using a calibrated stereo rig comprising two cameras, taking pictures at 640x480 pixel resolution. The cameras were calibrated using a checkerboard. The mean error of calibration was 0.33 pixels, corresponding to a maximum of 1.18 mm. Registration was performed using Matlab *procrustes* algorithm to estimate the homogeneous transformation matrices that transform the camera and EM-based measurements to a global coordinate system fixed at the base of the robot (shown in Fig. 3). The resulting root

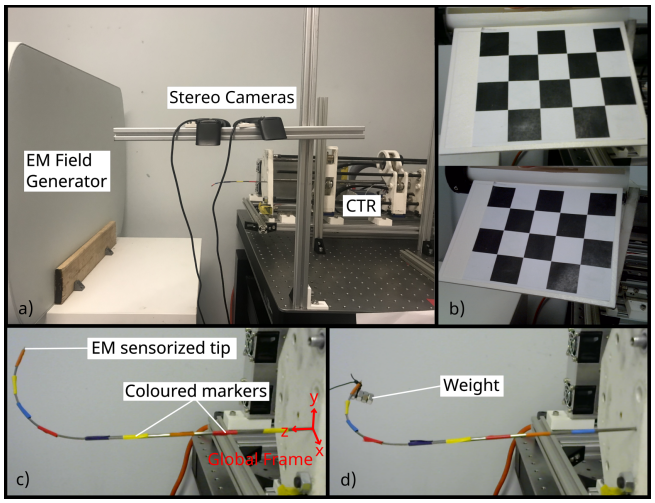

Fig. 3. a) Experimental setup. b) A checkerboard pattern was used to calibrate the stereo camera pair. c) A close-up image of the CTR. d) A CTR with weight attached to the tip.

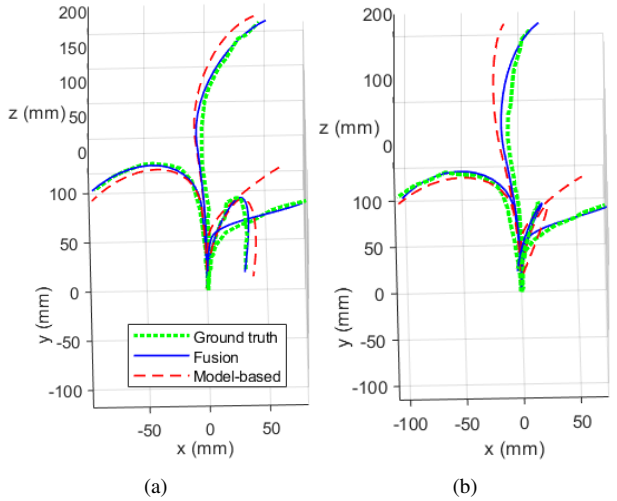

Fig. 4. Representative experimental results for shape estimation in (a) static experiments without force, and b) the equivalent test cases with added 11g weight. The results show a comparison between observer-based shape estimation, the baseline model-based shape estimation, and the ground truth.

mean squared errors of registration were 1.7mm and 5.5mm for the EM sensor and camera measurements, respectively.

During the experiments, coloured markers were attached to the robot backbone. Marker edges, as well as the start and end points of the robot were manually selected in both images and triangulated to reconstruct the 3D shape of the robot. The reconstructed shapes were used as ground truth throughout the experiments to verify the accuracy of the shape estimation algorithm.

The extracted 3D backbones were used to calibrate for the CTR model parameters, namely, Young's and shear moduli of the tubes. The parameters were identified by fitting the kinematic model given in (1) to the shape of the robot estimated via the cameras at 10 different configurations. The parameters of the model are given in Table I. The maximum error of the model in predicting the robot's tip position was smaller than 8% of the robot's arc length, achieving a similar performance to [4]. Moreover, a dataset of 10 shapes was used for tuning the observer parameters, namely Q and V. Q and V values were tuned to $3 \times 10^4 \times \mathbf{I}$ and $1.48 \times 10^3 \times \mathbf{I}$, respectively. These values were found to achieve the minimum shape estimation error.

TABLE I
CTR MODEL'S PARAMETERS.

Parameters	Tube 1	Tube 2
Length [mm]	505	251
E [GPa]	37.26	63.57
G [GPa]	34.39	53.68
I $[m^4]$	6.01×10^{-14}	3.267×10^{-13}
U_1 $[m^{-1}]$	14	2.8
U_2 $[m^{-1}]$	0	0

We performed three sets of experiments:

1) Static experiments, where the robot is moved to 17 different positions across its workspace. The observer was used to estimate the shape of the robot, giving enough time to converge in each static case.
2) Static experiments were repeated with attached 7 g and 11 g weights on the tip of the robot to simulate the effects of tissue interaction. Force magnitudes are similar to the tissue interaction forces preceding tissue puncture in needle-based interventions [20]. The dataset consisted of the same 17 configurations that were used in the previous experiment.
3) Dynamic experiments were performed on a moving CTR. The tubes were rotated 360° at 10.2°/sec and translated 40 and 20 mm at 1.1 and 0.6 mm/sec velocity. The estimated initial curvature of the robot $u(0, t_k)$ at each a time t_k was used as the guess in the next sample time t_{k+1}.

In all the experimental scenarios, we measured the performance of the observer and the baseline model given in (1) with two errors: E_r, measuring the prediction of the robot's tip, and E_{shape}, which is the error of the robot's full shape. Both errors are calculated by comparing the observer and the model-based predictions with the 3D reconstructed camera shape:

$$E_r = ||r_N - r_N^{gt}||, \tag{21a}$$

$$E_{shape} = \sqrt{\frac{1}{N}\sum_{n=1}^{N} \left|\left|r_n - r_n^{gt}\right|\right|^2}, \tag{21b}$$

where r_n and r_n^{gt} are the positions of the n^{th} point on the robot's backbone with $n = 0$ starting from the robot's base, describing the observed and ground truth shapes, respectively. In the cases where the observed and ground truth shapes are described by different numbers of points, we sample a subset of points from a denser shape which are the closest in distance to the corresponding points on a sparser shape. This is a preferred method over interpolation because it does not modify ground truth.

Fig. 4 shows representative experimental results in static experiments with and without force. The observer-based shape estimation is compared with the ground truth data

TABLE II

MEAN, STANDARD DEVIATION, MAX, AND NORMALISED MEAN OF ERRORS E_r AND E_{shape}.

		E_r				E_{shape}			
Weight	Method	Mean [mm]	Std [mm]	Max [mm]	Norm [%]	Mean [mm]	Std [mm]	Max [mm]	Norm [%]
$0g$	Observer	6.46	3.42	12.45	2.87	5.37	1.13	7.92	2.39
	Baseline	16.96	9.21	35.72	7.54	9.36	4.14	17.87	4.16
$7g$	Observer	6.89	3.40	11.37	3.06	5.40	1.62	7.94	2.40
	Baseline	21.96	9.70	41.11	9.76	10.85	4.46	19.51	4.82
$11g$	Observer	7.36	3.57	12.99	3.27	5.61	1.59	8.59	2.49
	Baseline	17.05	9.13	32.40	7.58	9.19	4.03	17.05	4.08

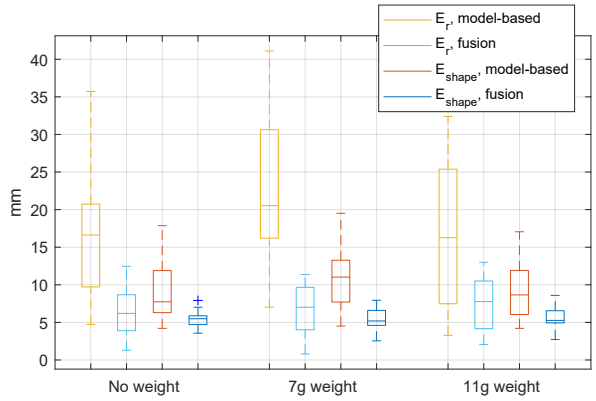

Fig. 5. Error bars comparing the observer to the baseline method. Starting from the middle of the box, the line inside the box corresponds to the median error, box ends indicate the 25^{th} and 75^{th} percentiles, and the ends of the dashed lines are the maximum and minimum errors.

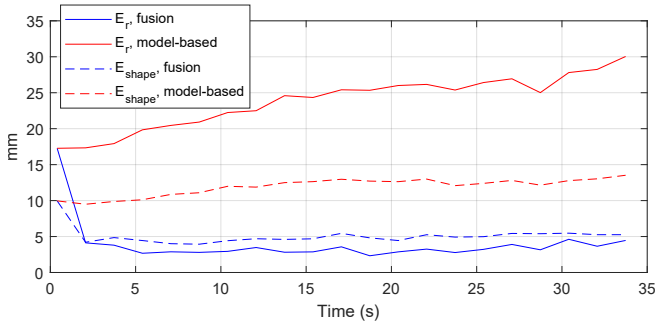

Fig. 6. E_r and E_{shape} progression through time while the robot is moving. Moving velocity is 5.9mm/s.

measured using the stereo camera pair. To demonstrate the performance of the observer in reducing CTR model's errors, we presented the model-based prediction as well, simulated using (1).

Experimental results for the static scenarios are summarised in Fig. 5 and Table II for 17 trials with and without external force. Errors for the tip and shape predictions for both the baseline model and the observer are reported. Table II also shows normalised mean errors as percentages of the robot's arc length, which is 225mm at default tube translation parameters. The observer can estimate the shape of the CTR without external force with a 5.37mm error, which corresponds to 2.39% of the robot's arc length. It improves model-based prediction error of shape by 42.6%. Similarly, in experiments with external force, the observer outperforms the baseline model prediction that benefits from the exact knowledge of the force's magnitude and orientation by an average of 45.1% without any a-priori knowledge of the external force. Moreover, as opposed to the model-based baseline prediction, the observer offers a consistent error in all cases as evident by the standard deviation of error. Thus, the observer offers a reliable estimation across the robot's workspace.

To demonstrate the real-time performance of the observer, we used it to predict the robot's shape while it was moving. The average tip velocity was approximately 5mm/s. The observer sampling time was set to 0.15 sec. Fig. 6 shows the evolution of tip error E_r and shape error E_{shape} for the baseline model and the observer. Observer errors rapidly converge to a value below 6mm, while the model-based predictions remain consistently large.

Moreover, we evaluated the observer's performance while the CTR was moving at different velocities. The same movement sequence was tested at 10 different velocities ranging from 5.9 to 54.8 mm/s. Tip position error E_r and shape error E_{shape} of the observer with respect to the tip velocity and time normalised by maximum travelling time are shown in Fig. 7.

As it can be seen the observer's error rapidly converges to a small value as time passes and linearly increases with respect to the robot velocity. This shows that the observer requires enough time to adapt to the changes in the feedback signal and is most suitable for control of the CTR at lower velocities below 10 mm/sec, which is appropriate for medical interventions. It should be noted that the current implementation of the algorithm has not been optimized for high-speed computation. However, many components of the algorithm including tensor multiplications can be parallelized. Thus, the computational time of the algorithm would benefit from using multicentral-processing-unit-based implementations.

The results demonstrate that the performance of the proposed shape estimation algorithm is comparable to other shape estimation approaches that employ medical image modalities or FBG sensors without suffering from the previously discussed drawback of those methods. For instance, Vandini *et. al* reported 7.28mm tip position error for a vision-based based method [6], while Khan *et. al* reported mean tip position error of 4.69 mm for multicore FBG-based shape estimation [13]. We note that the proposed method relies on the Cosserat rod model and can be generalised to many types of continuum robots which are modelled by Cosserat-rod theory. Finally, the observer unifies the robot's tracking, shape estimation, and solving the kinematic model in real-time offering a real-time shape sensing platform for

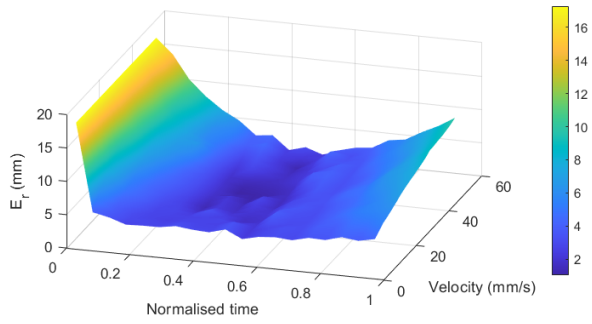

(a)

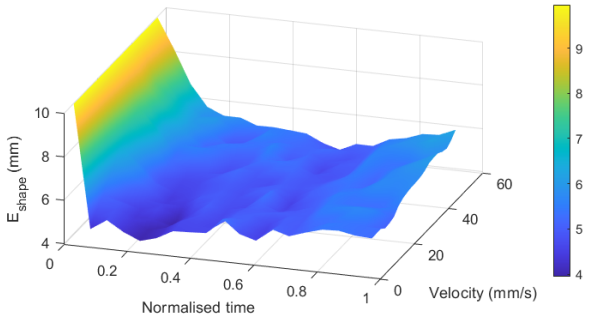

(b)

Fig. 7. a) E_r and b) E_{shape} progression trough time at different velocities.

control of CTRs using model-based approaches such as model predictive control.

IV. Concluding Remarks

We presented a fusion algorithm to estimate the shape of concentric tube robots. The approach combines a kinematic model of the robot with a single point measurement of the robot's tip given by an electromagnetic tracker. Compared to other shape sensing modalities, the presented methodology is easy to integrate and offers a low-cost and reliable solution for shape sensing of concentric tube robots. The performance of the shape sensing algorithm was experimentally validated with a series of experiments with and without external force. The mean error of the observer in predicting the robot's shape was 2.43% of the robot's arc length. The observer was capable of improving model-based shape predictions by 44.3%. The presented framework proved to be more robust and accurate than the kinematic model even without the knowledge of external contact forces. Furthermore, it was shown that the algorithm maintains similar performance in real-time while the robot is moving at velocities below 10mm/s.

References

[1] J. Burgner-Kahrs, D. C. Rucker, and H. Choset, "Continuum robots for medical applications: A survey," *IEEE Transactions on Robotics*, vol. 31, no. 6, pp. 1261–1280, 2015.

[2] T. da Veiga, J. H. Chandler, P. Lloyd, G. Pittiglio, N. J. Wilkinson, A. K. Hoshiar, R. A. Harris, and P. Valdastri, "Challenges of continuum robots in clinical context: a review," *Progress in Biomedical Engineering*, vol. 2, no. 3, p. 032003, aug 2020.

[3] P. E. Dupont, J. Lock, B. Itkowitz, and E. Butler, "Design and control of concentric-tube robots," *IEEE Transactions on Robotics*, vol. 26, no. 2, pp. 209–225, 2010.

[4] D. C. Rucker, B. A. Jones, and R. J. Webster III, "A geometrically exact model for externally loaded concentric-tube continuum robots," *IEEE Transactions on Robotics*, vol. 26, no. 5, pp. 769–780, 2010.

[5] E. J. Lobaton, J. Fu, L. G. Torres, and R. Alterovitz, "Continuous shape estimation of continuum robots using x-ray images," in *2013 IEEE International Conference on Robotics and Automation*, 2013, pp. 725–732.

[6] A. Vandini, C. Bergeles, F.-Y. Lin, and G.-Z. Yang, "Vision-based intraoperative shape sensing of concentric tube robots," in *2015 IEEE/RSJ International Conference on Intelligent Robots and Systems (IROS)*, 2015, pp. 2603–2610.

[7] A. Vandini, C. Bergeles, B. Glocker, P. Giataganas, and G.-Z. Yang, "Unified tracking and shape estimation for concentric tube robots," *IEEE Transactions on Robotics*, vol. 33, no. 4, pp. 901–915, 2017.

[8] R. J. Roesthuis, M. Kemp, J. J. van den Dobbelsteen, and S. Misra, "Three-dimensional needle shape reconstruction using an array of fiber bragg grating sensors," *IEEE/ASME Transactions on Mechatronics*, vol. 19, no. 4, pp. 1115–1126, 2014.

[9] M. Abayazid, M. Kemp, and S. Misra, "3d flexible needle steering in soft-tissue phantoms using fiber bragg grating sensors," in *2013 IEEE International Conference on Robotics and Automation*, 2013, pp. 5843–5849.

[10] R. J. Roesthuis, S. Janssen, and S. Misra, "On using an array of fiber bragg grating sensors for closed-loop control of flexible minimally invasive surgical instruments," in *2013 IEEE/RSJ International Conference on Intelligent Robots and Systems*, 2013, pp. 2545–2551.

[11] R. J. Roesthuis and S. Misra, "Steering of multisegment continuum manipulators using rigid-link modeling and fbg-based shape sensing," *IEEE Transactions on Robotics*, vol. 32, no. 2, pp. 372–382, 2016.

[12] S. C. Ryu and P. E. Dupont, "Fbg-based shape sensing tubes for continuum robots," in *2014 IEEE International Conference on Robotics and Automation (ICRA)*, 2014, pp. 3531–3537.

[13] F. Khan, A. Donder, S. Galvan, F. R. y. Baena, and S. Misra, "Pose measurement of flexible medical instruments using fiber bragg gratings in multi-core fiber," *IEEE Sensors Journal*, vol. 20, no. 18, pp. 10 955–10 962, 2020.

[14] S. Tully, G. Kantor, M. A. Zenati, and H. Choset, "Shape estimation for image-guided surgery with a highly articulated snake robot," in *2011 IEEE/RSJ International Conference on Intelligent Robots and Systems*, 2011, pp. 1353–1358.

[15] H. Sadjadi, K. Hashtrudi-Zaad, and G. Fichtinger, "Fusion of electromagnetic trackers to improve needle deflection estimation: Simulation study," *IEEE Transactions on Biomedical Engineering*, vol. 60, no. 10, pp. 2706–2715, 2013.

[16] A. Denasi, F. Khan, K. J. Boskma, M. Kaya, C. Hennersperger, R. Göbl, M. Tirindelli, N. Navab, and S. Misra, "An observer-based fusion method using multicore optical shape sensors and ultrasound images for magnetically-actuated catheters," in *2018 IEEE International Conference on Robotics and Automation (ICRA)*, 2018, pp. 50–57.

[17] F. Alambeigi, S. Aghajani Pedram, J. L. Speyer, J. Rosen, I. Iordachita, R. H. Taylor, and M. Armand, "Scade: Simultaneous sensor calibration and deformation estimation of fbg-equipped unmodeled continuum manipulators," *IEEE Transactions on Robotics*, vol. 36, no. 1, pp. 222–239, 2020.

[18] J. Wu, B. Li, C. Li, Y. Qiu, Z. Zhang, W. Lyu, A. Ali, S. A. H. Mohsan, W. Ge, Z. Tong, *et al.*, "Fiber bragg grating-based shape sensing: a review and perspective," in *Global Intelligent Industry Conference 2020*, vol. 11780. International Society for Optics and Photonics, 2021, p. 117801F.

[19] F. Callier and J. Willems, "Criterion for the convergence of the solution of the riccati differential equation," *IEEE Transactions on Automatic Control*, vol. 26, no. 6, pp. 1232–1242, 1981.

[20] M. Khadem, C. Rossa, R. S. Sloboda, N. Usmani, and M. Tavakoli, "Mechanics of tissue cutting during needle insertion in biological tissue," *IEEE Robotics and Automation Letters*, vol. 1, no. 2, pp. 800–807, 2016.